

Experimental and numerical studies of the flow over a circular cylinder at Reynolds number 3900

Philippe Parnaudeau,^{1,2} Johan Carlier,¹ Dominique Heitz,¹ and Eric Lamballais^{2,a)}

¹Cemagref, UR TERE, F-35044 Rennes, France and Université européenne de Bretagne, France

²Laboratoire d'Etudes Aérodynamiques UMR 6609, Université de Poitiers, ENSMA, CNRS Téléport 2-Bd. Marie et Pierre Curie B.P. 30179, 86962 Futuroscope Chasseneuil Cedex, France

(Received 2 January 2008; accepted 3 June 2008; published online 1 August 2008)

This work contributes to the study of flow over a circular cylinder at Reynolds number $Re=3900$. Although this classical flow is widely documented in the literature, especially for this precise Reynolds number that leads to a subcritical flow regime, there is no consensus about the turbulence statistics immediately just behind the obstacle. Here, the flow is investigated both numerically with large eddy simulation and experimentally with hot-wire anemometry and particle image velocimetry. The numerical simulation is performed using high-order schemes and a specific immersed boundary method. The present study focuses on turbulence statistics and power spectra in the near wake up to ten diameters. Statistical estimation is shown to need large integration times increasing the computational cost and leading to an uncertainty of about 10% for most flow characteristics considered in this study. The present numerical and experimental results are found to be in good agreement with previous large eddy simulation data. Contrary to this, the present results show differences compared to the experimental data found in the literature, the differences being larger than the estimated uncertainty range. Therefore, previous numerical-experimental controversy for this flow seems to be reduced with the data presented in this article. © 2008 American Institute of Physics. [DOI: 10.1063/1.2957018]

I. INTRODUCTION

Flow over circular cylinders is a simple and useful model for many applications concerning obstacles to flow. This classic case encapsulates all the complexity of the topology of the flow by preserving the potentially unstable regions where turbulence is generated. These regions are the boundary layer on the obstacle, the two shear layers delimiting the recirculation region, and the wake. The behavior of the flow in the wake depends on the state of these regions which can be laminar, transitional, or turbulent according to the Reynolds number Re ($Re=U_c D/\nu$, where U_c is the external velocity, D the diameter of the circular cylinder, and ν is kinematic viscosity). Despite this geometric simplicity, the circular shape of the cylinder is a challenge for numerical study. Indeed, there is no sharp edge that selects *a priori* the location of flow separation. This location is only fixed by the flow regime or the upstream conditions. For this reason, numerical predictions of turbulence statistics in the near region are very sensitive and can lead to significant discrepancies according to the methods used.

For $Re \in [400, 200\,000]$ transition to turbulence proceeds toward the circular cylinder and takes place in the shear layers. Norberg¹ suggested that this subcritical flow regime range exhibits a lower and upper parts with a basic change at $Re=5000$. Prasad and Williamson² confirmed this change at $Re=5000$ by studying the relation between the Reynolds number Re and the Strouhal number St ($St=f_{vs}D/U_c$, where f_{vs} is the vortex shedding frequency). Ra-

jagopalan and Antonia³ analyzed with power spectra the behavior of the vortex shedding in the wake and the Kelvin-Helmholtz instability in the shear layer. They invoke a less organized vortex shedding for $Re > 5000$. Transition to turbulence takes place in the boundary layers only for $Re > 200\,000$ corresponding to the supercritical regime.

The subcritical flow regime is close to industrial configurations involved in the food industry where wake flow must be controlled in order to deliver localized ultraclean air. More fundamentally, moderate Re flow regime is accessible both experimentally and numerically by highly resolved large eddy simulation (LES). For this reason, the $Re=3900$ case is probably the more documented one in the literature and can be viewed as a generic benchmark for the subcritical regime. The present work is a contribution to the knowledge of this flow by providing new reference data in near wake region ($0 < x/D < 10$) that could be useful for further studies on this subject.

From an experimental point of view, there are relatively few hot-wire anemometry (HWA) measurements available in the near wake of the circular cylinder owing to the presence of the recirculation zone and high instantaneous flow angles up to $x/D=10$. Despite these experimental difficulties, Ong and Wallace⁴ managed to accurately measure velocity and vorticity vectors with a complex wire probe in the near wake outside the recirculation bubble ($3 < x/D < 10$) at $Re=3900$ by the use of a look-up table data reduction technique. They propose turbulence statistics and power spectra of the streamwise and normal fluctuating velocity components at several locations. Additionally, Rajagopalan and Antonia³ performed HWA measurements in shear layers but only for

^{a)}Electronic mail: lamballais@univ-poitiers.fr.

power spectra analysis and not for turbulence statistic quantification.

To avoid the restrictions associated with the presence of back flow, the techniques of particle image velocimetry (PIV) or laser Doppler velocimetry (LDV) are more appropriate. Lourenco and Shih⁵ performed very early in the PIV history, time resolved measurements at $Re=3900$ in the recirculation region of the flow behind a circular cylinder accelerated up to a constant velocity in the water. Statistical quantities were assessed even if this PIV experiment was not designed for this purpose. Nevertheless, these results are often used as reference for the validation of many numerical simulations (for example, Beaudan and Moin,⁶ Kravchenko and Moin,⁷ or Ma *et al.*⁸). Lin *et al.*⁹ examined with PIV the flow behind circular cylinder for $1000 < Re < 10\,000$. They used instantaneous, phase, and time-averaged velocity and vorticity fields to investigate the structure of the separated shear layer and the vortex formation length. Noca *et al.*¹⁰ computed statistical profiles with their PIV experiments and focused their attention on the behavior of the vortex formation length according to the Reynolds number for $300 < Re < 4000$. They brought together a lot of data and observed a slight influence of the aspect ratio on the vortex formation length. Norberg¹¹ carried out LDV experiments in the near wake ($0 < x/D < 7$) for $1500 < Re < 10\,000$, but not exactly for $Re=3900$. Turbulence statistics were obtained for streamwise and normal fluctuating velocity components at several locations. Length scales were identified from the location of extreme values for these quantities. Dong *et al.*¹² investigated the very near wake with PIV and direct numerical simulation (DNS) at $Re=3900/4000$ and $10\,000$. They present a PIV/DNS comparison of mean and turbulent isocontour maps and focus on shear layer instability with their DNS data.

In the context of numerical simulation, Beaudan and Moin⁶ were the first to perform LES of flow at $Re=3900$. They solved the filtered Navier–Stokes equations for a slightly compressible flow using fifth-order upwind-biased and sixth-order centered finite difference schemes for the discretization of convective and viscous terms, respectively. The influence of the numerical dissipation caused by upwind schemes and also the influence of subgrid scale model are considered. Outside the recirculation region, the profiles of mean velocity and Reynolds stresses obtained are in reasonable agreement with the results of Lourenco and Shih.⁵ Inside the recirculation zone, discrepancies are observed, especially for the streamwise velocity profiles. Beaudan and Moin⁶ attributed these discrepancies to the experiment of Lourenco and Shih's whose statistics deviate from symmetric and antisymmetric conditions required by the flow configuration. Beaudan and Moin⁶ concluded from spectral analysis of their data that upwind-biased numerical schemes affect small scale turbulences in the wake so that the contribution of the subgrid scale model does not appear to be significant outside the recirculation region. Further downstream, the dynamic model is found to predict more accurately mean velocities and Reynolds stresses. Mittal and Moin¹³ performed a LES of the same flow using second-order conservative central-difference schemes. The results are in reasonable

agreement with the simulations of Ref. 6 and the experiments of Refs. 4 and 5. By the examination of power spectra of velocity fluctuations, Mittal and Moin¹³ concluded that nondissipative schemes are more appropriate for LES of this type of flow. Similarly, Mittal and Moin¹³ disagree with Lourenco and Shih's experiments in the recirculation region. For instance, the numerical simulations predict the U-shape mean velocity profile in the near-wake region whereas Lourenco and Shih measured a V-shape profile at the same location. This disagreement between experimental and numerical data was confirmed by the LES of Kravchenko and Moin⁷ who found a U-shape mean velocity profile.

More recently, Ma *et al.*⁸ attempted to resolve conflicting experimental and numerical results available in the literature by performing several DNSs and LESs with the Smagorinsky eddy viscosity model at $500 < Re < 5000$. Their algorithm is based on a new class of spectral/hp methods on unstructured grids. Their mean velocity profiles converge to a U-shape when the spanwise length of the computational domain is πD , whereas a V-shape is observed by Ma *et al.*⁸ using a twice extended domain in the spanwise direction. This behavior suggests a strong uncertainty regarding the value of the formation length (see Noca *et al.*¹⁰). Their power spectra have an inertial subrange that spans more than half a decade of wavenumbers if the grid resolution is not too low and the subgrid-scale dissipation is not too high. Mahesh *et al.*¹⁴ developed a finite-volume algorithm for LES with the Smagorinsky model on unstructured grids. They generalize the Harlow–Welch formulation for unstructured grids. Flow at $Re=3900$ was chosen for validation. Global variables such as recirculation length, Strouhal number, separation point, mean velocities and turbulent Reynolds stresses are shown to be in good agreement with previous LES. Breuer¹⁵ studied the numerical and modeling parameters that influence the quality of LES solutions at $Re=3900$. The best agreement with previous experiments is obtained with the less dissipative numerical schemes, and to a lesser degree, with the dynamic rather than the fixed-coefficient Smagorinsky model. In accordance with Moin and co-workers,^{6,14,16} doubling the domain in the spanwise direction does not affect the results significantly, contrary to the results of Ma *et al.*⁸

Previous numerical simulations use body-fitted (curvilinear or unstructured) grids which are designed to follow the shape of the wall in contact with the fluid. The advantage of this strategy is the possibility to locally refine the grid near the cylinder while imposing accurately the no-slip condition at the wall. The drawbacks are the difficulty in the numerical code development, the computational cost, and the loss of accuracy introduced by the grid distortion. An alternative to the body-fitted approach is the immersed boundary method (IBM). This technique is an attractive compromise in terms of simplicity, computational cost, and accuracy because the use of high-order finite difference schemes is straightforward in a simple Cartesian grid. The loss of accuracy is then concentrated in the near-wall region depending on the quality of the forcing method used to mimic the no-slip condition and also on the mesh size near the wall that cannot be adjusted easily to the shape of the obstacle.

In this paper, the flow over a circular cylinder is studied

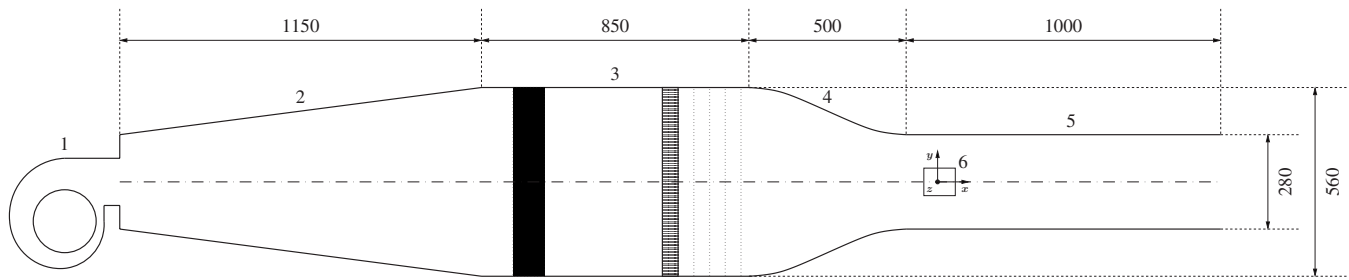


FIG. 1. Cross-section view of the wind tunnel.

in the near wake ($0 < x/D < 10$) at the “generic” Reynolds number $Re=3900$. This study is conducted both numerically with LES and experimentally with HWA and PIV. The purposes of this paper are twofold: (i) to carry out with PIV a detailed investigation in the very near wake of a circular cylinder and (ii) to show the aptitude of an IBM associated with LES to give reliable results. Throughout this article, the comparison between the data obtained from these two different methodologies is used to evaluate the relevancy of the data presented here.

II. EXPERIMENTAL SETUP

The experiments were conducted in one of the wind tunnels at the Rennes Regional Center of Cemagref with PIV and HWA.

A. Wind tunnel

The cross-section view of the wind tunnel used in the experiments is presented in Fig. 1. The wind tunnel is mainly made up of a centrifugal fan, a diffuser, a plenum chamber with honey comb and grids, a contraction section that decreases by 4, and a testing zone with transparent walls. The testing zone is square in the cross section with a width of $H=28$ cm and a length of 100 cm. The upper wall is slightly tilted to suppress the longitudinal pressure gradient. The flow velocity can be chosen continuously between 1 and 8 m s^{-1} with a good precision. The uniformity of the velocity profile at the entrance of the wind tunnel was checked by HWA (see Fig. 2). The free stream turbulence intensity is less than 0.2%. The temperature is kept within ± 0.2 °C by using an air-water heat-exchanger located at the fan inlet. Note that this location is of secondary importance for the present wind tunnel situated in a well thermally isolated room so that the heat balance can stabilize the temperature everywhere.

The circular cylinder has a length $L=280$ mm and a diameter $D=12$ mm. It is equipped with two thin rectangular end plates with the specification recommended by Stansby.¹⁷ The distance between the end plates is 240 mm providing an aspect ratio $L/D=20$. The clearance between the walls and the end plates is about of 20 mm which is much larger than the thickness of the boundary layer. The blockage ratio is 4.3%. The circular cylinder is mounted horizontally at $3.5D$ from the entrance of the testing zone.

The longitudinal axis x is the testing zone axis of the wind tunnel. The spanwise axis z is the circular cylinder axis.

The normal axis (normal to the symmetry plane of the wake) follows the Cartesian right-hand rule. The origin is located at the center of the circular cylinder.

B. PIV measurements

2D2C PIV experiments (to in-plane velocity components in a plane field) were carried out with a NewWave laser Solo 3 based on neodymium-doped yttrium aluminum garnet (Nd:YAG) with an energy pulse of 50 mJ and two PCO cameras SensiCam (CCD size of 1280×1024 pixel, pixel size of $6.7 \times 6.7 \mu\text{m}^2$, and dynamics of 12 bits). The laser sheet is

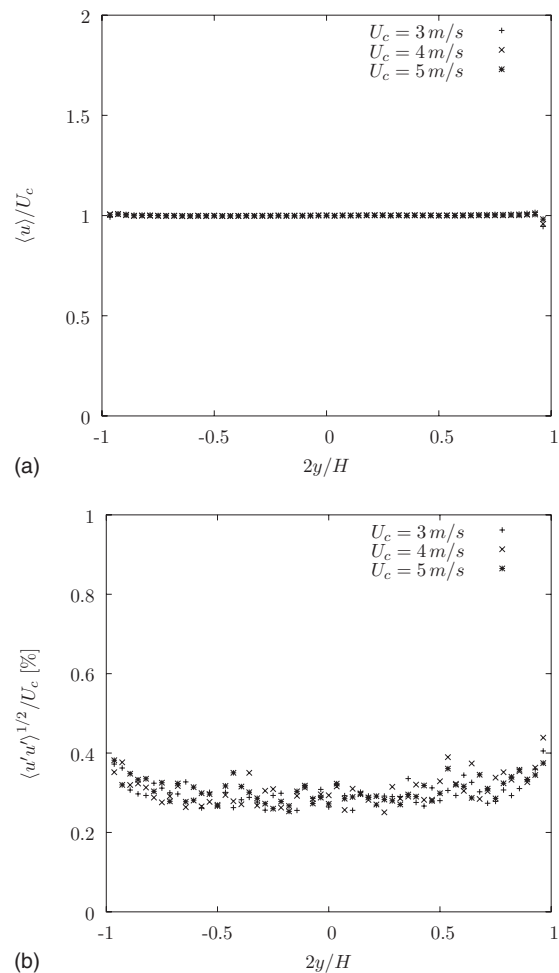


FIG. 2. At the entrance of the testing zone of the wind tunnel. Left: Uniformity of the flow. Right: Free stream turbulence intensity.

carried out with a Rodenstock telescope and a cylinder lens. The diameter of the particle seeding (diluted polyglycol in water) is less than 10 μm . The main experiment is 2D2C PIV measurements at the plane $z=0$ just behind the circular cylinder. The first camera is located perpendicularly on one side of the laser sheet at a distance of 36 cm and the second camera on the other side at a distance of 23 cm. The same type of lens (focal length of 50 mm and aperture of 5.6) is mounted on both cameras. The fields of view are $3.6D \times 2.9D$ for the first camera (case 1) and $1.9D \times 1.6D$ for the second (case 2). The free stream velocity is adjusted to 4.8 m s^{-1} so that the Reynolds number Re is 3900. There are 5000 image pairs for each camera obtained with a time interval of 25 μs between two successive images. The statistical profiles presented hereafter come from case 2, except for the maps in Fig. 16 and the longitudinal profiles in Figs. 9 and 10 where case 1 is added (large field of view). Moreover, an extra PIV experiment was carried out in the plane $z/D=0$ from which only one vorticity map is used hereafter (Fig. 4).

The PIV records were analyzed by cross correlation using fast-Fourier-transform algorithm in a multigrid process with three iterations and shift subpixel (64×64 , 32×32 , and 16×16 pixel) and 50% overlapping. The cross-correlation peaks are fitted with a Gaussian function on 3 pixels. Erroneous velocity vectors are identified by a median filter and are replaced by a local mean value. To give an idea of the present experiment accuracy, the particle displacement range is about -2 to $+7$ pixel in case 1 and -4 to $+14$ pixel in case 2 (with an error less than 0.3 pixel on the instantaneous displacement, typical for this kind of PIV method¹⁸) and less than 0.1% of the velocity vectors are erroneous.

C. HWA measurements

Using the same experimental configuration as previously described, the wake behind a circular cylinder is explored by HWA. The experiment was carried out with a X -wire probe (Dantec 55P61 in platinum plated tungsten with 5 μm diameter, 1.25 mm length, and 1 mm separation). The probe is connected to a constant-temperature anemometer (2 CTA module 90C10 in a Streamline 90N10 frame). Each bridge is equipped with a gain and an offset to adjust the output voltage to an A/D converter (National Instruments PCI-MIO-16E-4) and a sample and hold (National Instruments SC-2040). The X -wire probe was calibrated both in velocity and angle with a compressed-air driven jet (Dantec flow unit 90H02) using cosine-law method.

The sampling frequency is 6000 Hz and the analog low-pass filter cutoff frequency is 3000 Hz. The number of samples is 204 800 with a recording length of 34 s. The experiment consisted of measuring four velocity profiles at the locations $x/D=3, 5, 7,$ and 10 for $y/D \in [-5; +5]$ with a step $\Delta y/D=0.1$. The experiment lasted 2 h for each (u, v) and (u, w) probe orientations. For this type of HWA experiment, the uncertainty estimations of the statistics are about of 1% and 4% for the first- and second-order moments, respectively (see Carlier and Stanislas¹⁸ for details).

III. NUMERICAL METHODOLOGY

A. Governing equations

Following the classical framework of LES, the filtered incompressible Navier–Stokes equations considered are

$$\frac{\partial \bar{u}_i}{\partial t} + \left(\frac{\partial \bar{u}_i}{\partial x_j} - \frac{\partial \bar{u}_j}{\partial x_i} \right) \bar{u}_j = - \frac{1}{\rho_0} \frac{\partial \bar{p}_m}{\partial x_i} + \nu \frac{\partial^2 \bar{u}_i}{\partial x_j \partial x_j} + f_i + \frac{\partial T_{ij}}{\partial x_j}, \quad (1)$$

$$\frac{\partial \bar{u}_i}{\partial x_i} = 0, \quad (2)$$

where ρ_0 is the (constant) density, \bar{p}_m the modified/filtered pressure, and \bar{u}_i the filtered velocity components in Cartesian coordinates x_i . The forcing term f_i corresponds to the modeling of the no-slip condition at the cylinder surface through the IBM (see the next section for details). The subgrid-scale tensor T_{ij} is approximated here using the structure function model proposed by Métais and Lesieur.¹⁹ This eddy viscosity model is used in its simplest formulation with the fixed constant model ($C_F=0.105C_k^{3/2}$) of Métais and Lesieur¹⁹ combined with a fixed filter length estimated as the cubic root of the mesh volume. Note that in the preliminary tests, we have checked that for the high spatial resolution used here (close to the one expected for a DNS), more sophisticated subgrid-scale models do not seem to be required.

B. General description of the code

The incompressible Navier–Stokes equations are solved on a regular Cartesian grid in nonstaggered configuration. Sixth-order compact centered difference schemes are used to evaluate all spatial derivatives, except near, in- and outflow boundaries where single sided schemes are employed for the x -derivative calculation. Time integration is performed with a second-order Adams–Bashforth scheme. A constant flow is imposed at the inlet of the computational domain while a simple convection equation is solved at the exit. Periodic conditions are used in the two lateral directions y and z . For more details about the numerical code and its validation in the context of the DNS of complex jets and wakes, see Lardeau *et al.*,²⁰ Silvestrini and Lamballais,²¹ and Lamballais and Silvestrini.²²

As already stated in the previous section, the forcing term f_i represents the IBM used to impose the no-slip condition at the cylinder surface. Several formulations were proposed in the literature with various names (see Mittal and Iaccarino,²³ for a review). In this work, we use a direct forcing approach.²⁴ The basic idea of this technique is to directly apply the target velocity \bar{u}_{i0} to the solution in the forcing region. To understand how this method can be easily implemented, it is useful to consider the temporal discretization of Eq. (1) for a time step $\Delta t = t_{n+1} - t_n$,

$$\frac{\bar{u}_i^{n+1} - \bar{u}_i^n}{\Delta t} = \frac{3}{2} \bar{F}_i^n - \frac{1}{2} \bar{F}_i^{n-1} - \frac{1}{\rho_0} \frac{\partial \bar{p}_m^{n+1}}{\partial x_i} + \tilde{f}_i^{n+1}, \quad (3)$$

where

$$\bar{F}_i = - \left(\frac{\partial \bar{u}_i}{\partial x_j} - \frac{\partial \bar{u}_j}{\partial x_i} \right) \bar{u}_j + \nu \frac{\partial^2 \bar{u}_i}{\partial x_j \partial x_j} + \frac{\partial T_{ij}}{\partial x_j},$$

while the time integrated values of the filtered pressure and forcing term are, respectively,

$$\bar{p}_m^{n+1} = \frac{1}{\Delta t} \int_{t_n}^{t_{n+1}} \bar{p}_m dt, \quad \tilde{f}_i^{n+1} = \frac{1}{\Delta t} \int_{t_n}^{t_{n+1}} f_i dt.$$

Within this framework, the direct forcing method leads to the expression

$$\tilde{f}_i^{n+1} = \varepsilon \left(-\frac{3}{2} \bar{F}_i^n + \frac{1}{2} \bar{F}_i^{n-1} + \frac{1}{\rho_0} \frac{\partial \bar{p}_m^{n+1}}{\partial x_i} + \frac{\bar{u}_i^{n+1} - \bar{u}_i^n}{\Delta t} \right), \quad (4)$$

with $\varepsilon=1$ in the body and 0 everywhere else. A well known drawback of IBM is the creation of spurious oscillations in the neighborhood of the wall where no slip is mimicked. This nonphysical behavior is amplified by the use of a direct forcing combined with high-order centered schemes, as it is done in this study. For this reason, following the formulation proposed and validated by Parnaudeau *et al.*²⁵ for the DNS of the same flow at $Re=300$, a specific definition of the target velocity \bar{u}_{i_0} is used in order to improve the regularity of the solution in the neighborhood of the cylinder surface. To present the formulation of this target velocity, it is convenient to use cylindrical coordinates (r, θ, z) for which, for instance, the no-slip condition can be written as

$$\bar{u}_{i_0}(D/2, \theta, z, t) = 0. \quad (5)$$

The principle of the present forcing is to create an internal flow preserving the no-slip boundary at the cylinder surface while avoiding strong discontinuities of the first derivatives at $r \approx D/2$. The more straightforward method to ensure this second property is to impose inside the cylinder a reverse flow similar to mirror conditions with respect to $r=D/2$. Following this idea, the target velocity field is calibrated according to the external flow through the formal expression

$$\bar{u}_{i_0}(r, \theta, z, t) = -g(r) \bar{u}_i(D-r, \theta, z, t), \quad (6)$$

with

$$g(r) = \sin\left(\frac{2\pi r^2}{D^2}\right). \quad (7)$$

The use of a modulation function $g(r)$ is necessary to avoid singularity at $r=0$. Note that the choice of the exact expression of $g(r)$ is rather arbitrary providing that this function remains smooth with $g(0)=0$ (singularity cancellation), $g(D/2)=1$ (reverse condition near the cylinder surface), and $g(r) \in [0:1]$.

Because the target velocity given by Eq. (6) is not divergence-free, the incompressibility condition must be modified inside the cylinder in order to allow a mass source/sink. This can be performed by replacing the incompressibility condition by

$$\frac{\partial \bar{u}_i}{\partial x_i} = \frac{\partial(\varepsilon \bar{u}_{i_0})}{\partial x_i} \quad (8)$$

that differs from Eq. (2) only in the forcing region where the created flow is purely artificial. Note that since in practice the target velocity is defined on the Cartesian grid, an interpolation procedure is necessary to apply approximately the condition (6). Due to the approximate nature of the IBM, the no-slip condition can be ensured only up to second-order accuracy, so that a bilinear interpolation is simply used in this work.

Returning to the time discretization, the forcing procedure is implemented through a three step advancement,

$$\frac{\bar{u}_i^* - \bar{u}_i^n}{\Delta t} = \frac{3}{2} \bar{F}_i^n - \frac{1}{2} \bar{F}_i^{n-1} - \frac{1}{\rho_0} \frac{\partial \bar{p}_m^n}{\partial x_i} + \tilde{f}_i^*, \quad (9)$$

$$\frac{\bar{u}_i^{**} - \bar{u}_i^*}{\Delta t} = \frac{1}{\rho_0} \frac{\partial \bar{p}_m^n}{\partial x_i}, \quad (10)$$

$$\frac{\bar{u}_i^{n+1} - \bar{u}_i^{**}}{\Delta t} = -\frac{1}{\rho_0} \frac{\partial \bar{p}_m^{n+1}}{\partial x_i}, \quad (11)$$

with the target velocity $\bar{u}_{i_0}^{n+1}$ estimated by

$$\bar{u}_{i_0}^*(r, \theta, z, t) = -g(r) \bar{u}_i^*(D-r, \theta, z, t) \quad (12)$$

and

$$\tilde{f}_i^* = \varepsilon \left(-\frac{3}{2} \bar{F}_i^n + \frac{1}{2} \bar{F}_i^{n-1} + \frac{1}{\rho_0} \frac{\partial \bar{p}_m^n}{\partial x_i} + \frac{\bar{u}_{i_0}^* - \bar{u}_i^n}{\Delta t} \right). \quad (13)$$

Note that the forcing is actually applied on \bar{u}_i^* instead of \bar{u}_i^{n+1} [see Eqs. (9) and (13)], resulting in a splitting error proportional to Δt^2 so that the second-order accuracy of the full time advancement is preserved. Finally, the last pressure gradient correction is carried out using the solution of the following pressure equation:

$$\frac{1}{\rho_0} \frac{\partial^2 \bar{p}_m^{n+1}}{\partial x_i \partial x_i} = \frac{1}{\Delta t} \frac{\partial((1-\varepsilon) \bar{u}_i^{**})}{\partial x_i}, \quad (14)$$

that is compatible with the condition (8) while corresponding to the conventional Poisson equation outside the cylinder and to the Laplace equation in the artificial flow region inside the cylinder. The accuracy of this specific IBM, especially the benefit of the creation of an internal flow ensuring the regularity of the solution when high-order centered schemes are used, is discussed in detail by Parnaudeau *et al.*²⁵

C. Flow parameters

Our computational domain extends over $20D$ in the streamwise and normal directions. The spanwise extent of the domain was chosen to be $L_z = \pi D$, which corresponds to the size used by most of previous authors. The center of the cylinder is located at $x_{\text{cyl}} = 5D$ downstream from the inlet section where a purely constant (in time and space) and unidirectional longitudinal flow of velocity U_c is imposed. Table I gives the grid resolution and the comparison between the LES and PIV dimension parameters. The main numerical

TABLE I. Principal characteristics of LES and PIV.

	Re	$L_x \times L_y \times L_z$	$\Delta t U_c / D$	TU_c / D (shed. periods)	$n_x \times n_y \times n_z$
LR LES	3900	$20D \times 20D \times \pi D$	0.006	2020 (420)	$481 \times 480 \times 48$
HR LES	3900	$20D \times 20D \times \pi D$	0.003	250 (52)	$961 \times 960 \times 48$
Wind tunnel	...	$66D \times 23D \times 23D$
PIV case 1	3900	$1.9D \times 1.6D$	160×128
PIV case 2	3900	$3.6D \times 2.9D$	160×128

results shown in this paper are obtained from a high resolution LES (HR LES). Additionally, a low resolution LES (LR LES) is also presented to evaluate the grid sensitivity while allowing us to consider the convergence level of statistical data through the very long time integration. A fixed time step is used in order to ensure the Courant–Friedrich–Levy restriction, with $\Delta t = 0.003D/U_c$ for HR LES and $\Delta t = 0.006D/U_c$ for LR LES.

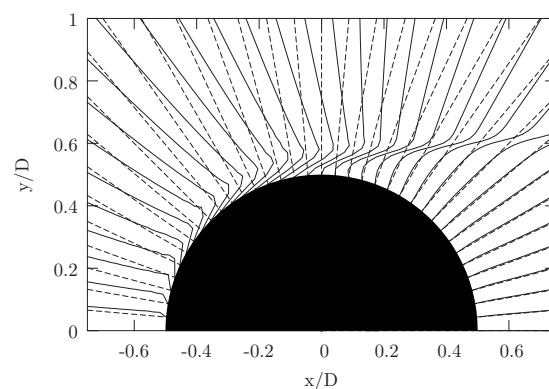
At this stage, it is necessary to introduce the discussion about the relevancy of the spatial resolution. Since we use a Cartesian grid that is regular in the three directions of space, present mesh sizes ($\Delta x, \Delta y, \Delta z$) can be easily deduced. Contrary to the resolution in the z -direction that is similar to the one used by previous authors with $\Delta z \approx 0.065D$,²⁵ the grid used here is particularly large in the two other directions near the cylinder, with $\Delta x = \Delta y \approx 0.021D$ for HR LES and $\Delta x = \Delta y \approx 0.042D$ for LR LES. Typically, in previous LES based on body fitted grid, the grid is strongly refined near the cylinder in order to describe very accurately the development and detachment of the boundary layer. Here, we adopt the opposite point of view by using a regular grid that leads to a better spatial resolution in the active region of the flow (up to the far wake) while being significantly less accurate for the description of the boundary layer. In the present flow regime where the boundary layer remains fully laminar, the use of a nonrefined near-wall spatial resolution can be accepted by assuming that the influence of the detailed structure of the boundary layer on the wake statistics is rather weak. This conjecture will be checked *a posteriori* in Sec. IV C where experimental and numerical results will be compared. In other words, while previous authors used refined spatial discretization to describe the near-wall flow, we choose here to use a purely regular grid that offers an excellent description of the coherent structures, but only outside from the near-wall region. The use of a regular grid, initially motivated by its simplicity and efficiency in terms of computational cost and numerical development, is a strength of the present LES that will be commented again in the section dedicated to the analysis of results. To give an idea about the resolution of the boundary layer in the near-cylinder region, the mean tangential velocity profile $\langle u_\theta \rangle$ obtained by HR LES is presented in Fig. 3. Cartesian to cylindrical transformation was performed with a bicubic interpolation based on 3×3 points and with the origin located at the center of the cylinder. This picture illustrates well the verification of the no-slip condition at the wall and the growth of the boundary layer around the cylinder. The boundary layer thickness increases from the stagna-

tion point up to the separation point (at $\theta \approx 88^\circ$, in agreement with the values collected in the literature by Franke and Frank²⁶). At the separation point, the boundary layer is only described with about five grid points across its thickness estimated as the region where the mean velocity norm is less than 99% of U_c . Naturally, an equivalent description of boundary layers cannot be expected from LR LES. The impact of this very crude boundary layer representation on statistics will be examined in the following.

IV. RESULTS

First, samples of instantaneous flow fields are presented in order to describe briefly the structure of the flow. Spectra and other statistical results are then compared to those of the following.

- Ong and Wallace:⁴ HWA experiment with aspect ratio about $L/D=84$ ($D=14.3$ mm) and $Re=3900$.
- Norberg:¹¹ LDV experiment with aspect ratio about $L/D=65$ ($D=6$ mm) and $Re=3000$ and 5000 .
- Lourenco and Shih:⁵ PIV experiments described by Beaudan and Moin.⁶ This experiment is resolved in time and photographs are taken at a frequency of 6 Hz, during 29 vortex shedding cycles. Aspect ratio is about $L/D=21$ and $Re=3900$.
- Kravchenko and Moin:¹⁶ LES at $Re=3900$ using a multizone grid corresponding to a single-zone O-type grid of $n_r \times n_\theta \times n_z = 205 \times 185 \times 48$ points covering the domain $R_d \times L_z = 60D \times \pi D$. Incompressible Navier–Stokes equations are solved with a Galerkin

FIG. 3. Mean tangential velocity profile $\langle u_\theta \rangle$ around the circular cylinder.

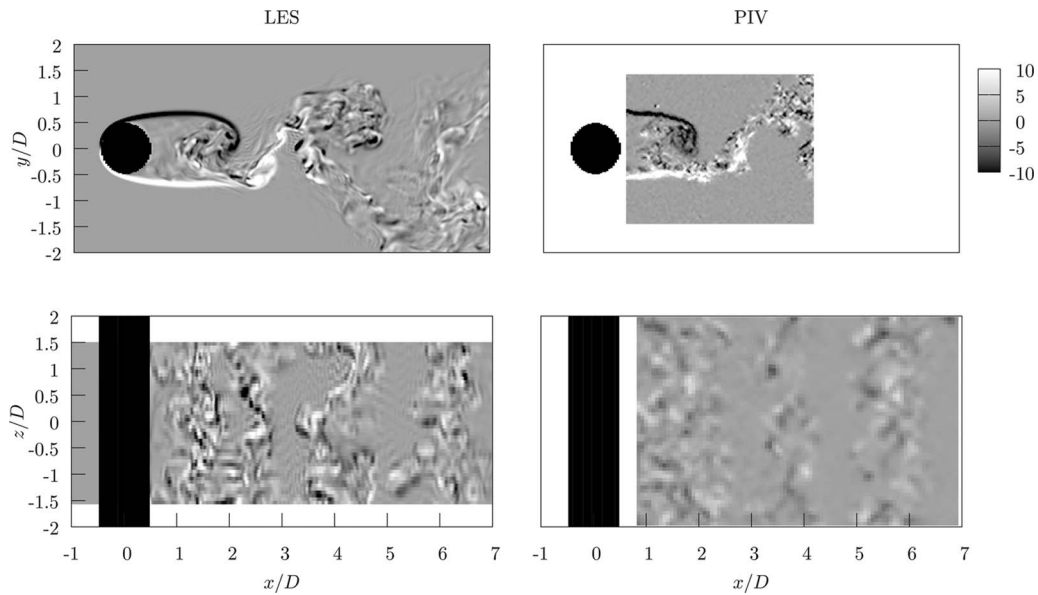


FIG. 4. Experimental and numerical comparisons between maps of spanwise $\omega_z D/U_c$ (top) and normal $\omega_y D/U_c$ (bottom) instantaneous vorticity components.

B-spline method with a dynamic Smagorinsky subgrid-scale model.

- Ma *et al.*:⁸ DNS at $Re=3900$ on a unstructured grid using spectral/hp method. The domain size is $L_x \times L_y \times L_z = 40D \times 18D \times \pi D$ (case II) with a resolution corresponding to 5×10^7 degrees of freedom.
- Dong *et al.*:¹² (i) PIV experiments in free-surface water channel at $Re=4000$. The circular cylinder is equipped with end plates. The aspect and blockage ratio are about of $L/D=8.78\%$ and 8.3% . 600 velocity fields are used to compute statistics; (ii) DNS at $Re=3900$ employing an unstructured grid of 902 spectral elements (eight order Jacobi polynomial expansions) in the streamwise-crossflow planes and 96 Fourier modes in the spanwise direction. The domain size is $L_x \times L_y \times L_z = 40D \times 18D \times 1.5\pi D$. Statistical quantities are accumulated on 40–50 shedding cycles.

In the present LES, the turbulent wake has been considered as fully established (loss of the initial conditions) after a duration of $T=150D/U_c$. All statistics presented here are computed after this transient stage over a different time for LR LES and HR LES (see Table I). Statistics are also averaged in the periodic spanwise direction. The averaging operator is denoted by $\langle \cdot \rangle$. A discussion about the convergence level of the present statistical data can be found in Sec. IV C.

A. Instantaneous flow field

Figure 4 presents the spanwise ω_z and normal ω_y components of the instantaneous vorticity in two symmetry planes ($y=0$ and $z=0$). These vorticity fields have been arbitrarily selected in the PIV and HR LES databases so that they illustrate the same flow topology.

In the plane $z=0$, HR LES and PIV present an equivalent range for the apparent vorticity magnitude and scales (the colors shading off is strictly the same for both experimental and numerical maps). The noise level for PIV measurements

remains relatively weak despite the high resolution used in space (final window size of 16×16 pixels). The spanwise vorticity ω_z highlights the two shear layers on both sides of the cylinder. At the end of the recirculation zone, the top shear layer becomes unstable and rolls up to form a primary vortex. Small vortices resulting from the instability of the shear layer seem to accumulate in this primary large scale structure. The bottom shear layer is almost straight and laminar up to $x/D=2$. This scenario is observed alternatively in the two shear layers and at different stages of their evolution in the instantaneous fields. The Bénard–von Karman vortex street begins further downstream with two shedding cycles visible in the field of view of HR LES results in Fig. 4.

In the plane $y=0$, the field of view of the PIV measurement is more extended than the previous plane. Consequently, the scale range is narrower so that small scales cannot be identified as well as for HR LES. Downstream from the cylinder, alternate turbulent and irrotational regions show the presence of the Bénard–von Karman vortex street with a quasi-two-dimensional (2D) shedding mainly parallel to the cylinder. The end plates described in Sec. II A have been used to decrease the effects of the boundary layer (which develops on the wall of the wind tunnel) on the wake flow. The alignment of the end plates with the main flow has been adjusted carefully to avoid a tilt effect on the occurrence of oblique and dislocation modes as observed by Prasad and Williamson.²⁸

These instantaneous flow fields show the fully three-dimensional character of the dynamics where a wide range of scales can be observed. The primary vortex shedding can be clearly identified while being submitted to small scale fluctuations, in agreement with Kravchenko and Moin.¹⁶ The longitudinal vortices cannot be easily identified in Fig. 4 only based on two vorticity components. The visualization of vorticity modulus ω_n (colored by the longitudinal vorticity component ω_x) obtained with the HR LES emphasizes more clearly the presence of these longitudinal vortices (cf. Fig. 5)

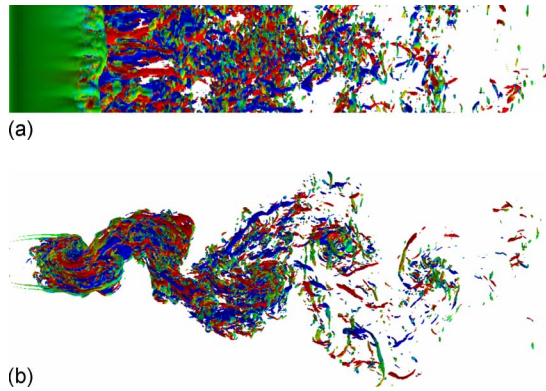


FIG. 5. (Color online) Isosurface of instantaneous vorticity modules $\omega_n = 8U_c/D$ colored by the longitudinal vorticity ω_x in top and side views.

that are mainly responsible of the three-dimensional motions in the domain considered. As it has already been observed in previous studies, the longitudinal vortices are created through a stretching process between the Karman vortices that remain mainly parallel to z -direction.

B. Frequency spectra

Figures 6 and 7 show power spectra of streamwise and normal velocity fluctuations at four locations downstream from the cylinder and on the centerline of the wake. Power spectra are estimated with the periodogram technique. In HR LES study, the number of sample available is 83 304, corresponding to a time duration $T=250D/U_c$ of about ≈ 52 vortex shedding cycles. Power spectra are estimated using two sequences of 39 vortex shedding overlapped at 67%. All the 48 points in the spanwise direction z are treated as independent and used to average the power spectra. In HWA study, the periodogram technique is applied with 219 sequences of

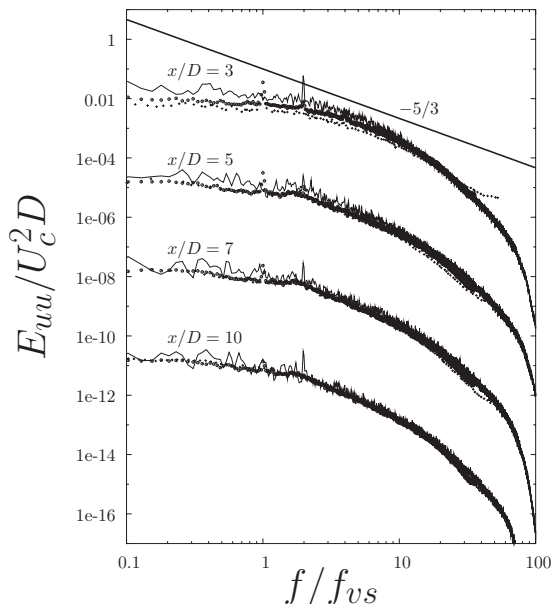


FIG. 6. Power spectra of the streamwise velocity fluctuations at four locations (the first at $x/D=3$ is not shifted). (—) Present HR LES; (○) present HWA experiment; (+) experiment of Ong and Wallace (Ref. 4).

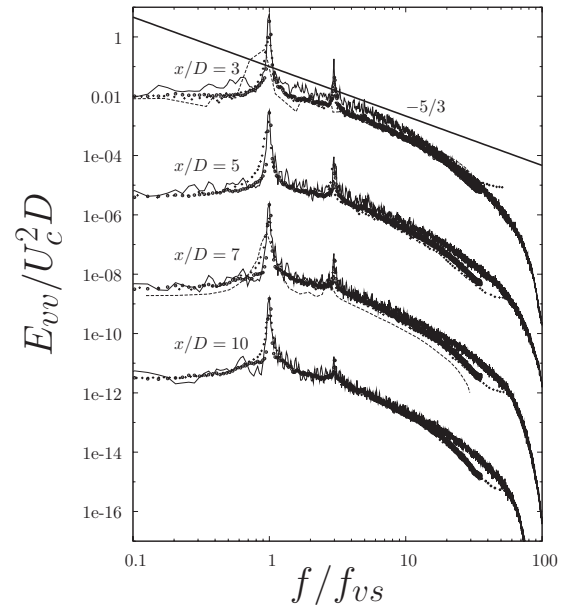


FIG. 7. Power spectra of the normal velocity fluctuations at four locations (the first at $x/D=3$ is not shifted). (—) Present HR LES; (○) present HWA experiment; (+) experiment of Ong and Wallace (Ref. 4); (- - -) Ma *et al.* (Ref. 8) case I.

39 vortex shedding overlapped at 67%. The same Hanning window has been used for the numerical and experimental data. All the power spectra are shown nondimensionalized and compared to results of Ong and Wallace.⁴

Globally, both the present and Ong and Wallace⁴ HWA experiments yield very similar power spectra, this agreement being a convincing validation of the present experimental methodology. The overall agreement with LES is also very satisfactory.

The Strouhal numbers used to define the nondimensional frequency f/f_{vs} for the spectra presented in Figs. 6 and 7 are estimated as $St=0.208 \pm 0.002$ for HWA and $St = 0.208 \pm 0.001$ for HR LES. For HWA, the main contribution to the uncertainty on St is due to the uncertainty on the inflow mean velocity U_c that can be measured only with a relative accuracy of about 1%. For HR LES, the uncertainty is associated with the limited extent of the time sequence. Here, the estimation of the Strouhal number is obtained through the direct examination of the time history of the velocity data due to the well marked periodic behavior of the flow. Hence, locating the first and last peaks of the v' time history on the full temporal sequence recorded experimentally or numerically, the number of vortex shedding can be counted unambiguously through the direct examination of the signal so that an estimation of the Strouhal frequency accurate up to 0.01% for HWA (confirming that this uncertainty source can be neglected) and 0.5% for HR LES.

Peaks at the fundamental ($f/f_{vs}=1$) and second harmonic ($f/f_{vs}=3$) frequencies are very pronounced for the v -spectra, whereas the first harmonic does not appear on the centerline. Note that this second harmonic is also well marked further downstream for x -locations (not shown). Ong and Wallace⁴ suggested that the occurrence of these peaks can be predicted by linear stability theory. For the u -spectra,

peaks are found to be clearly less marked while being partially the signature of a measure bias for HWA results. This bias can be detected through the presence of the peak at $f/f_{vs}=1$ that should not be present at the centerline, the only expected pronounced peak being at twice the vortex shedding frequency (see Ma *et al.*⁸). Here, we interpret the erroneous peak at $f/f_{vs}=1$ as a consequence of the cosine law and calibration methods used for the present HWA measurement that lead to a slight contamination of u by v . Note, however, that the expected peak $f/f_{vs}=2$ in u -spectra can be marginally observed for HWA results while being more pronounced for HR LES results.

An inertial subrange can be clearly observed for the u -spectra both for the present LES and experiments with nearly an extension of one decade at the station $x/D=5, 7$, and 10, this range being a little bit narrower at $x/D=3$. As was reported by Kravchenko and Moin,¹⁶ the spectra are also consistent with the presence of small scales that remain active far from the cylinder. These findings are consistent with the instantaneous flow visualizations presented in Fig. 4.

Ma *et al.*⁸ and Kravchenko and Moin¹⁶ noticed that the effect of an excessive dissipation leads to a rapid decay of the spectra so that no inertial subrange can be satisfactorily captured. Contrary to this, spectra obtained by LES based on nondissipative schemes better match the experiments. The agreement between present LES and experiments for a large spectral range, especially for high frequencies, confirms this trend in our numerical code while suggesting that the subgrid-scale modeling is not overdissipative. Moreover, the present use of a low resolution in the near-cylinder region does not seem to affect the quality of the spectra. This remark supports the idea that a very precise description of the boundary layer is not necessary to capture accurately the turbulent dynamics of the flow. This point will be confirmed in the next section where one-point statistics are analyzed.

C. First and second order statistics

To start this section, it is necessary to consider the statistical convergence expected for the present data. In practice, the averaging time used by previous authors to compute statistics can differ significantly from one study to another. For instance, Kravchenko and Moin¹⁶ have considered seven vortex shedding periods for their statistics, while Dong *et al.*¹² have used 40–50 vortex shedding cycles whereas Ma *et al.*⁸ used 131. To our knowledge, no numerical or experimental study about the convergence of the principal turbulence statistics is available in the literature. Franke and Frank²⁶ studied this point and noticed that more than 40 shedding periods are required to obtain converged mean flow statistics in the neighborhood of the cylinder. In preliminary tests, we have observed that the convergence level of a given set of statistical data is in practice very delicate to evaluate. For instance, we have been able to compute a set of first and second order statistics in excellent agreement with the present experimental data using only 12 shedding cycles from the present HR LES. A particularly misleading point is that mean and fluctuating velocity profiles can be remarkably well symmetric (with respect to $y=0$) despite the use of this

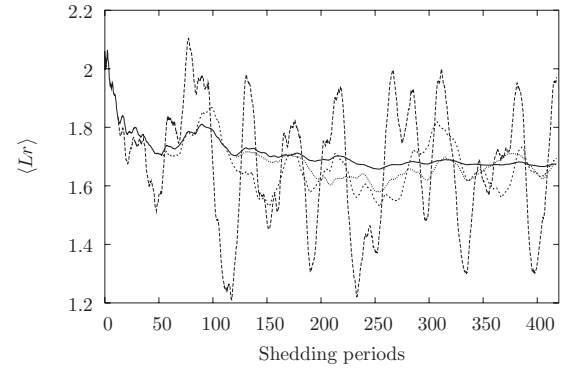


FIG. 8. Sensitivity of L_r with respect to the time integration: (—) cumulative [see Eq. (15)]; (---) sliding with $T=12$; (- · - ·) sliding with $T=52$; (····) sliding with $T=120$ shedding periods [see Eq. (16)].

limited time interval, suggesting erroneously that statistics are rather well converged. Unfortunately, if the same statistics are computed using an extended averaging time of 52 shedding periods, the agreement with experimental data remains satisfactory but is found to be less good. To better understand this behavior, we have computed statistics using only 12 shedding cycles on various time intervals distributed among the 52 available. As a first conclusion, we have observed that the quality of the prediction of the recirculation length L_r is the deciding factor about the agreement between experimental and numerical statistics. By definition, the recirculation length L_r corresponds to the distance between the base of the cylinder and the sign change of the centerline mean longitudinal velocity (see Fig. 9 for an illustration of this length). In other words, our experience is that an excellent statistical agreement between experiments and calculations can be exhibited using nonconverged LES data providing that the averaging time interval can lead to the right (from the experimental point of view) value of L_r .

As an introduction to the uncertainty associated with the present data, we have first focused on the sensitivity of L_r with respect to the averaging time interval. Due to the large number of shedding periods considered here, this preliminary study is only based on the LR LES for computational cost reasons. Figure 8 compares four curves showing the sensitivity of L_r with respect to the time sequence used in the average. By denoting the instantaneous value of the recirculation length $L_r(t)$ (deduced from the spanwise averaged longitudinal velocity at a given time t), four types of averaging operators are considered: a cumulative one defined by

$$\langle L_r \rangle_0^t(t) = \frac{1}{t} \int_0^t L_r(\tau) d\tau \quad \text{for } t \geq 0 \quad (15)$$

and three sliding ones with

$$\langle L_r \rangle_{t-T}^t(t) = \frac{1}{T} \int_{t-T}^t L_r(\tau) d\tau \quad \text{for } t \geq T, \quad (16)$$

where T is equal to 57, 248, and 571 corresponding to 12, 52, and 120 shedding periods, respectively. The examination of the curves $\langle L_r \rangle_0^t$ in Fig. 8 shows that no converged value of L_r can be expected for a time integration smaller than about

1200 time units, corresponding to 250 shedding cycles. Based on this cumulative average, a converged value can be proposed $L_r \approx 1.67$ with an uncertainty that is difficult to estimate. However, this estimation can be done approximately for shorter time integration by analyzing the behavior of sliding averages $\langle L_r \rangle_{t-T}^t$ presented in Fig. 8. The maximum deviation of these curves from the converged value $L_r \approx 1.67$ can provide a rough estimation of the uncertainty associated with the three time integrations considered. These assumptions lead to an uncertainties on L_r of about ± 0.5 , ± 0.2 , and ± 0.1 ($\pm 30\%$, $\pm 12\%$, and $\pm 6\%$) for 12, 52, and 120 shedding periods, respectively. In the rest of this article, we will consider statistical results collected over 52 shedding periods from the HR LES where we expect a similar uncertainty. Moreover, using the same procedure based on a sliding average on 52 shedding periods, we have recovered a relative uncertainty of about $\pm 10\%$ concerning the maximum values of fluctuating velocity components ($\langle u'u' \rangle_{\max}$, $\langle v'v' \rangle_{\max}$, and $\langle w'w' \rangle_{\max}$) at a given streamwise location. Despite the somewhat crude estimation of the present uncertainties, we will keep in mind this order of magnitude in the following comments comparing the experimental and numerical statistics.

Note that an additional LR LES has been performed to investigate preliminary the potential effect of the spanwise length of the computational domain. Since boundary conditions are periodic in this direction, the spanwise length of the cylinder is theoretically infinite but naturally, the length of periodicity can introduce an artificial constraint on the physics simulated. For this reason, we have conducted a complementary LR LES based on an extended computational domain in z -direction with $L_z = 2\pi D$ and $n_z = 96$, all the other numerical and physical parameters being identical to those of the standard LR LES reported in Table I. In agreement with previous studies,^{8,12} a 10% reduction of the recirculation length (computed using 100 vortex shedding cycles) is observed for the LR LES based on a z -extended domain. This sensitivity with respect to the length of periodicity in z -direction is only slightly larger than the expected uncer-

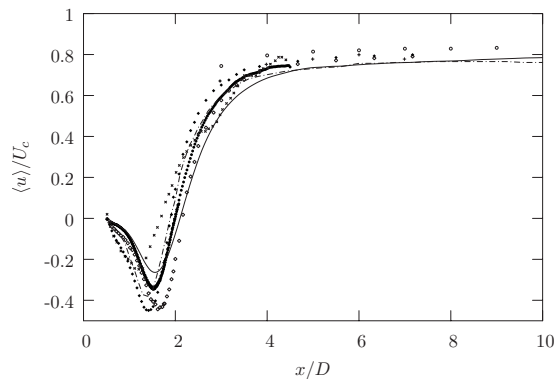


FIG. 9. Mean longitudinal velocity in the wake centerline of the circular cylinder at $Re=3900$: (—) present LES; (●) present PIV experiments (cases 1 and 2); (○) present HWA experiment; (---) B-spline simulations (case II) of Kravchenko and Moin (Ref. 16); (+) experiment of Ong and Wallace (Ref. 4); (×) experiment of Lourenco and Shih (Ref. 5); (◇) for $Re=3000$ and (◆) for $Re=5000$, experiment of Norberg (Ref. 11); (- - -) DNS of Ma *et al.* (Ref. 8) (case II).

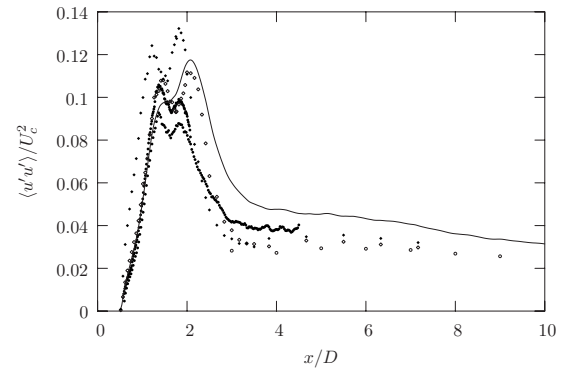


FIG. 10. Variance of the longitudinal velocity in the wake centerline. For details, see the caption for Fig. 9.

tainty. For this reason, and owing to the requirement for the time integration already discussed, we have chosen to select $L_z = \pi D$ for the HR LES that will be presented in the rest of the article. This choice means that the computational effort is concentrated on the statistical convergence instead of the degree of freedom of the simulated flow.

Figure 9 presents mean streamwise velocities in the wake centerline and Fig. 10 shows the variance. The mean streamwise velocity $\langle u \rangle$ on the wake centerline is zero at the base of the cylinder (no-slip condition). It reaches a negative minimum U_{\min} in the recirculation zone and converges asymptotically and monotonously toward the external velocity U_c . The variance of the streamwise velocity $\langle u'u' \rangle$ is also zero at the base of the cylinder and reaches two peaks before its slow monotonous decay toward zero. The formation length $L_{\langle u'u' \rangle}$ can be defined as the distance between the base of the cylinder and the x -location of the highest peak. Table II summarizes the mean flow parameters from measurements along the wake centerline.

Contrary to the L_r value, the LES and PIV do not provide the same U_{\min} value and deviate clearly from the interpolated U_{\min} value of Norberg.¹¹ It is known (as pointed out by Szepessy and Bearman,²⁹ Norberg,¹ Noca *et al.*¹⁰) that the L_r value is slightly dependent on the aspect ratio and/or blocking effects. U_{\min} value may be more sensitive to these effects that are less significant in the experiment of Norberg¹¹

TABLE II. Mean flow parameters: Re, Reynolds number; St, Strouhal number; L_r , recirculation length; U_{\min} , minimum of $\langle u \rangle$ on the centerline; $\langle u'u' \rangle_{\max}$, maximum of $\langle u'u' \rangle$ on the centerline; $L_{\langle u'u' \rangle}$, formation length.

	Re	St	L_r/D	U_{\min}/U_c	$L_{\langle u'u' \rangle}/D$
PIV	3900	...	1.51	-0.34	0.87
HWA	3900	0.208 ± 0.002
HR LES	3900	0.208 ± 0.001	1.56	-0.26	0.92
Ref. 5	3900	...	1.18	-0.25	...
Ref. 16, case II	3900	0.210	1.37	-0.35	...
Ref. 8, case II	3900	0.219	1.59
Ref. 11	3000	...	1.66	-0.44	0.95
Ref. 11	5000	...	1.40	-0.45	0.73
Ref. 12, PIV	4000	...	1.47	-0.252	...
Ref. 12, DNS	3900	0.203	1.36	-0.291	...

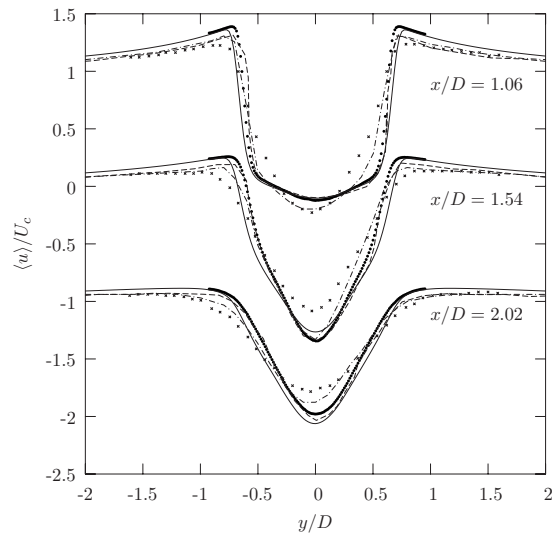


FIG. 11. Mean streamwise velocity at three locations in the wake of the circular cylinder at $Re=3900$. For details, see the caption for Fig. 9.

(aspect ratio of 65 and blocking of 1.5% for Norberg, 20 and 4.3% for the present results, and 8.78 and 8.3% for Dong *et al.*). The recirculation length of Lourenco and Shih⁵ is smaller than the other values. Kravchenko and Moin¹⁶ suggested that the smaller recirculation length is a consequence of an earlier transition in the shear layer due to inflow disturbances in the reference experiments. A lack of statistical convergence could also be suggested, since their PIV experiments have been conceived and optimized more for a dynamic study of the flow than for a statistical analysis.

In Fig. 10, $\langle u'u' \rangle$ from case 2 is much more in accordance with LES and Norberg's LDA data than from case 1. The accuracy of the case 2 (small field of view with $0.025D$ window size) is expected better than the case 1 (large field of view with $0.045D$ window size). Indeed, "cross-correlation window" of the PIV algorithm acts on the velocity field estimation as an average filter (see Foucaut *et al.*³⁰). The smaller is the window size, the better are estimated the turbulence statistics in the limit of the thickness of the laser sheet and the particle image concentration. For this reason, the statistical profiles presented hereafter come from case 2. The two peaks found previously by Norberg¹¹ in the $\langle u'u' \rangle$ centerline profile is supported by the present PIV experiment. There is no second peak in the present LES, but only a slight step. Even if the existence of the two peaks creates an uncertainty in the formation length estimation based on $\langle u'u' \rangle$, the values reported here are very similar. Norberg¹¹ believed that one of the two peaks is connected to the cross-over of mode-B longitudinal vortices, but it remains difficult to link clearly the occurrence of the local $\langle u'u' \rangle$ maxima to specific vortical events. To conclude this paragraph, it should be noticed that the characteristic lengths of the recirculation zone are very sensitive to limit conditions. Therefore, it may be interesting to supplement the knowledge of the impact of these conditions (especially aspect ratio and blocking effects) on these physical lengths.

Figure 11 shows profiles of mean streamwise velocities at three x -locations. As expected, a strong velocity deficit in

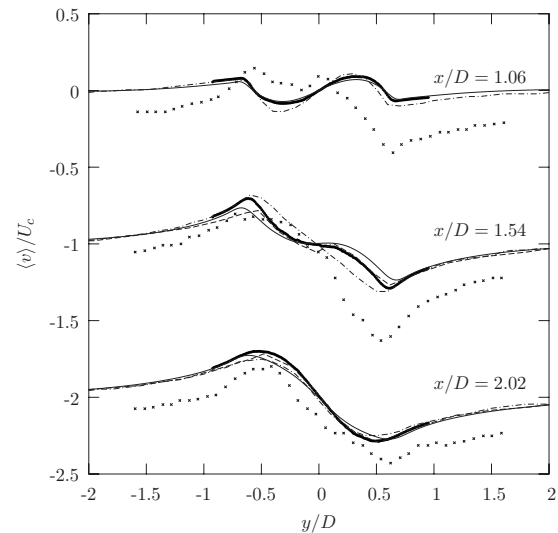


FIG. 12. Mean normal velocity at three locations in the wake of the circular cylinder at $Re=3900$. For details, see the caption for Fig. 9.

$\langle u \rangle$ profile occurs in the recirculation region with a U-shape close to the cylinder which evolves toward a V-shape further downstream. The identification of a U-shape in the very near wake is confirmed by the present results, both experimentally and numerically. The agreement between the present LES and experimental velocity profiles is very satisfactory while being comparable with previous LES.^{8,16} As already seen for recirculation length, the data of Lourenco and Shih⁵ deviate significantly from the LES results and also from the present experimental measures. Concerning the $\langle v \rangle$ data presented in Fig. 12, it is worth noting that all profiles verify the expected antisymmetry (with respect to $y=0$), except the data of Lourenco and Shih.⁵ This anomalous behavior suggests again that these measurements are influenced by some experimental disturbances, as already discussed.

Variance and covariance of the normal and streamwise velocity fluctuations at three locations in the wake are plotted in Figs. 13–15. At $x/D=1.06$, the $\langle u'u' \rangle$ -profile presents two strong peaks mainly due to the transitional state of the shear layers. As a possible contribution to these two peaks, a phenomenon of shear layer flapping can be suggested through the inflection of the shear layer by primary vortex formation. Note, however, that the two peaks are less pronounced in the present LES. This slight underestimation is probably due to the nonrefined mesh in the near-cylinder region, contrary to the other LESs where refined mesh is used in the region of shear layers. The flow is relatively quiet between the two peaks and becomes strongly agitated at the end of the recirculation zone where the primary vortices are generated. At $x/D > 1.06$, the two peaks of the shear layers are overlapped by two larger peaks due to primary vortex formation. Concerning the $\langle v'v' \rangle$ -profiles, their maximum occurs on the centerline, therefore it may be better to define the formation length with $\langle v'v' \rangle$ contrary to the common use. The Reynolds shear stress $\langle u'v' \rangle$ is antisymmetric, as for $\langle v \rangle$. To summarize, for all the profiles of the second order statistics presented here (see Figs. 13–15), the agreement between present LES and experimental data is very satisfactory and

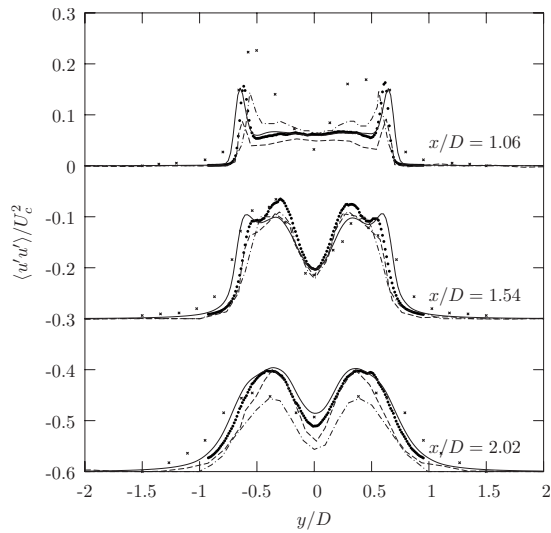


FIG. 13. Variance of the streamwise velocity fluctuations at three locations. For details, see the caption for Fig. 9.

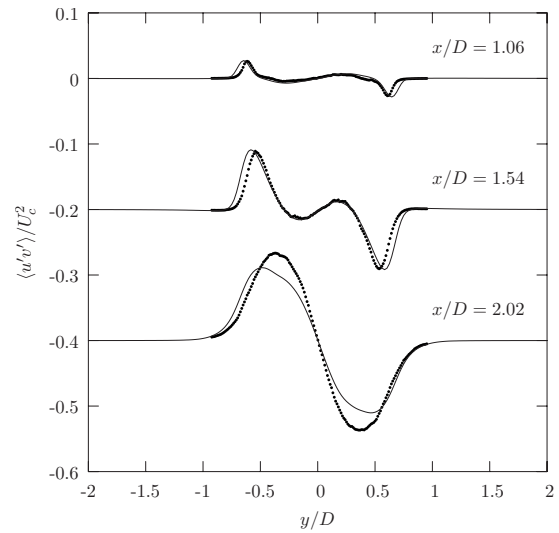


FIG. 15. Covariance of the velocity fluctuations at three x-locations. For details, see the caption for Fig. 9.

comparable with previous LES. Conversely, significant discrepancies with respect to the measurements of Lourenco and Shih⁵ are observed, as it was already stated by Refs. 8 and 16.

To confirm the quality of the present experimental/numerical agreement, 2D maps of first and second order statistics are shown in Fig. 16. This type of view allows a more complete observation of the data for which a large domain is covered (up to $x=4.5D$ for the experimental window). The $\langle u \rangle$ and $\langle u'u' \rangle$ maps emphasize the presence of the two shear layers. The $\langle u'u' \rangle$ is symmetric with a maximum value on either side of the wake centerline. Due to the two peaks in the $\langle u'u' \rangle$ centerline profile, there are two saddle points in the present PIV results (not shown by the isocontours in Fig. 16). The maximum of $\langle v'v' \rangle$ corresponds to a well defined and located peak on the centerline. The $\langle v \rangle$ and $\langle u'v' \rangle$ shapes

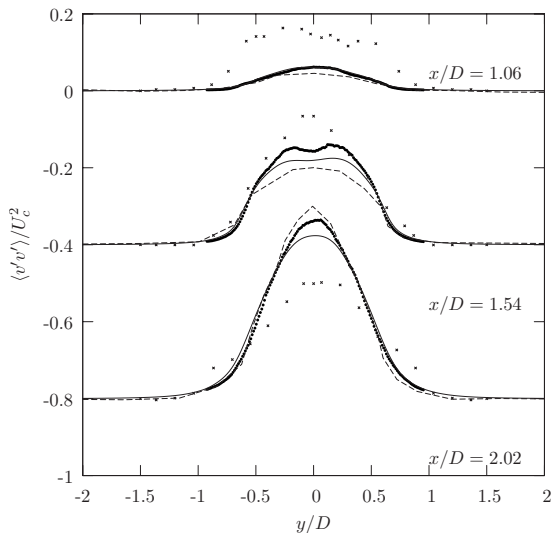


FIG. 14. Variance of the normal velocity fluctuations at three locations in the wake of the circular cylinder at $Re=3900$. For details, see the caption for Fig. 9.

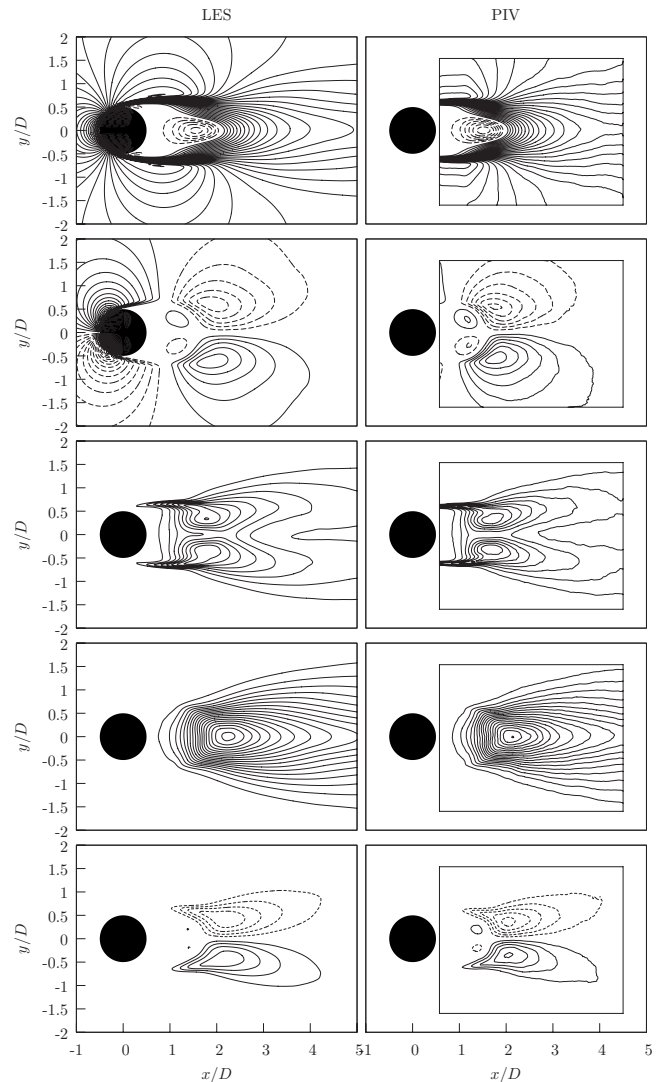


FIG. 16. Isocontour maps of the first and second order statistics: from top to bottom, $\langle u \rangle$, $\langle v \rangle$, $\langle u'u' \rangle$, $\langle v'v' \rangle$, and $\langle u'v' \rangle$ normalized with U_c or U_c^2 (left column, present LES; right column, present PIV).

are antisymmetric and look like a “butterfly” with two extrema on either side of the wake centerline. Note that these LES and PIV maps are in good mutual agreement and are also similar with those presented by Noca *et al.*¹⁰ at $Re=1260$ and by Dong *et al.*¹² at $Re=3900$ and $10\,000$.

V. CONCLUSION

The results from these experiments are complementary to each other. Together, the spatially resolved PIV data in the very near wake ($x/D < 3$) and the time resolved HWA data further downstream ($3 < x/D < 10$) yield a more complete picture. Particular attention was given to the accuracy and statistical convergence. Preliminary LESs have allowed us to estimate the statistical convergence within a relative uncertainty of $\pm 10\%$ on L_r when data are collected over a time of about 52 shedding periods. The present experimental results are in good agreement with the present LES, the deviation being smaller than the estimated uncertainty of $\pm 10\%$. Present statistics are found to be consistent with those of previous authors,^{6,14,16} in particular, concerning the recirculation region close to the cylinder. For the present LES, the use of a nonrefined grid in the near-cylinder region seems to be justified for this moderate Reynolds number. Indeed, for the subcritical regime, the boundary layer remains fully laminar, while downstream from its separation the shear layers are not too thin. Moreover, the quality of the results obtained by the association of an original IBM with high-order compact finite difference schemes is encouraging. It is worth emphasizing that the computational cost of the present LES is reasonable despite the high number of grid points used here. In fact, the use of Cartesian and regular grids significantly reduces the computing time per grid point, which is allowed by the IBM. Furthermore, without any additional numerical development, it should be possible to follow the same methodology for more complex obstacles, providing that the Reynolds number remains in the same range. This opportunity will be investigated in future studies where the effects of the shape of the cylinder will be considered in order to control the resulting wake flow. This work presents, for the first time to our knowledge, accurate experimental data that agree satisfactorily with the present and previous LES results for the generic case at $Re=3900$. Our work aids in the discussion over the controversy between experimental and numerical results. The authors hope that this study offers an extended database³¹ helpful for future experimental and numerical developments where the flow over a circular cylinder will probably remain a reference benchmark for a long time.

ACKNOWLEDGMENTS

The present LES was performed on the supercomputers of the IDRIS (the computational center of CNRS), to which we are thankful. The financial support by the Region of Bretagne in France under Grant No. 20048347 and by the European Union under Grant No. FP6-513663 are gratefully acknowledged. We wish to thank Christoffer Norberg for having kindly provided us his data and Steve Crittenden for correcting the English-written paper.

- ¹C. Norberg, “An experimental investigation of the flow around a circular cylinder: influence of aspect ratio,” *J. Fluid Mech.* **258**, 287 (1994).
- ²A. Prasad and C. H. K. Williamson, “Three-dimensional effects in turbulent bluff-body,” *J. Fluid Mech.* **343**, 235 (1997).
- ³S. Rajagopalan and R. A. Antonia, “Flow around a circular cylinder-structure of the near wake shear layer,” *Exp. Fluids* **38**, 393 (2005).
- ⁴J. Ong and L. Wallace, “The velocity field of the turbulent very near wake of a circular cylinder,” *Exp. Fluids* **20**, 441 (1996).
- ⁵L. M. Lourenco and C. Shih, “Characteristics of the plane turbulent near wake of a circular cylinder, a particle image velocimetry study,” published in Ref. 6 (1994).
- ⁶P. Beaudan and P. Moin, “Numerical experiments on the flow past a circular cylinder at sub-critical Reynolds number,” Technical report, CTR Annual Research Briefs, NASA Ames/Stanford University, 1994.
- ⁷A. G. Kravchenko, P. Moin, and K. Shariff, “B-spline method and zonal grids for simulations of complex turbulent flows,” *J. Comput. Phys.* **151**, 757 (1999).
- ⁸X. Ma, G.-S. Karamanos, and G. E. Karniadakis, “Dynamics and low-dimensionality of a turbulent near wake,” *J. Fluid Mech.* **410**, 29 (2000).
- ⁹J.-C. Lin, J. Towfighi, and D. Rockwell, “Instantaneous structure of the near-wake of a circular cylinder: on the effect of Reynolds number,” *J. Fluids Struct.* **9**, 409 (1995).
- ¹⁰F. Noca, H. G. Park, and M. Gharib, “Vortex formation length of a circular cylinder ($300 < Re < 4,000$) using DPIV,” in *Proceeding of FEDSM’98: 1998 ASME Fluids Division Summer Meeting, Washington, D.C., 1998* (ASME, Washington, D.C., 1998).
- ¹¹C. Norberg, “LDV-measurements in the near wake of a circular cylinder,” in *Proceedings of the Conference on Bluff Body Wakes and Vortex-Induced Vibration, Washington, D.C.*, edited by P. W. Bearman and C. H. K. Williamson (Cornell University, Ithaca, NY, 1998), pp. 1–12.
- ¹²S. Dong, G. E. Karniadakis, A. Ekmekci, and D. Rockwell, “A combined direct numerical simulation-particle image velocimetry study of the turbulent near wake,” *J. Fluid Mech.* **569**, 185 (2006).
- ¹³R. Mittal and S. Balachandar, “On the inclusion of three-dimensional effects in simulations of two-dimensional bluff-body wake flows,” *Proceedings of ASME Fluid Engineering Division Summer Meeting, Vancouver, British Columbia, Canada* (ASME, Vancouver, 1997).
- ¹⁴K. Mahesh, G. Constantinescu, and P. Moin, “A numerical method for large-eddy simulation in complex geometries,” *J. Comput. Phys.* **197**, 215 (2004).
- ¹⁵M. Breuer, “Large eddy simulation of the subcritical flow past a circular cylinder: numerical and modeling aspects,” *Int. J. Numer. Methods Fluids* **28**, 1281 (1998).
- ¹⁶A. G. Kravchenko and P. Moin, “Numerical studies of flow over a circular cylinder at $Re=3900$,” *Phys. Fluids* **12**, 403 (2000).
- ¹⁷P. K. Stansby, “The effects of end plates on the base pressure coefficient of a circular cylinder,” *Aeronaut. J.* **78**, 36 (1974).
- ¹⁸J. Carlier and M. Stanislas, “Experimental study of eddy structures in a turbulent boundary layer using particle image velocity,” *J. Fluid Mech.* **535**, 143 (2005).
- ¹⁹O. Métais and M. Lesieur, “Spectral large-eddy simulation of isotropic and stably stratified turbulence,” *J. Fluid Mech.* **239**, 157 (1992).
- ²⁰S. Lardeau, E. Lamballais, and J.-P. Bonnet, “Direct numerical simulation of a jet controlled by fluid injection,” *J. Turbul.* **105**, 354 (2002).
- ²¹J. H. Silvestrini and E. Lamballais, “Direct numerical simulations of wakes using virtual cylinders,” *Int. J. Comput. Fluid Dyn.* **16**, 305 (2002).
- ²²E. Lamballais and J. H. Silvestrini, “Direct numerical simulation of interactions between a mixing layer and a wake around a cylinder,” *J. Turbul.* **3**, 028 (2002).
- ²³R. Mittal and G. Iaccarino, “Immersed boundary methods,” *Annu. Rev. Psychol.* **37**, 239 (2005).
- ²⁴J. Mohd-Yusof, “Combined immersed boundaries/B-splines methods for simulations of a flows in complex geometries,” Technical Report, CTR Annual Research Briefs, NASA Ames/Stanford University, 1997.
- ²⁵P. Parnaudeau, E. Lamballais, D. Heitz, and J. H. Silvestrini, *Direct and Large-Eddy Simulation V* (Kluwer, Dordrecht, 2003), Vol. 9, pp. 581–590.
- ²⁶In preliminary calculations, we have checked that the use of $n_z=96$ grid points in spanwise direction has no significant effect on statistics (within the uncertainty range).
- ²⁷J. Franke and W. Frank, “Large eddy simulation of the flow past a circular cylinder at $Re=3900$,” *J. Wind. Eng. Ind. Aerodyn.* **90**, 1191 (2002).
- ²⁸A. Prasad and C. H. K. Williamson, “The instability of the shear layer separating from bluff body,” *J. Fluid Mech.* **333**, 375 (1997).

²⁹S. Szepessy and P. W. Bearman, "Aspect ratio and end plate effects on vortex shedding from a circular cylinder," *J. Fluid Mech.* **234**, 191 (1992).

³⁰J.-M. Foucaut, J. Carlier, and M. Stanislas, "Piv optimization for the study

of turbulent flow using spectral analysis," *Meas. Sci. Technol.* **15**, 1046 (2004).

³¹The experimental and numerical statistics presented in this article are available by contacting the authors.